Geophysical Journal International

Geophys. J. Int. (2026) **244,** 1–14
https://doi.org/10.1093/gji/ggaf495
Advance Access publication 2025 December 10
Research Paper

Induced polarization effects in fixed-wing airborne EM: the TEMPEST™ system—Part A, connecting numerical modelling with field evidence at continental scale

F. Dauti ,[1] Y. Ley Cooper,[2] T. Munday,[3] A. Viezzoli[4] and G. Fiandaca [1]

[1] *The EEM Team for Hydro & eXploration, Department of Earth Sciences A. Desio, University of Milan, Milano, 20133, Italy. E-mail: francesco.dauti@unimi.it*
[2] *Geoscience Australia, Canberra, ACT 2609, Australia*
[3] *The Commonwealth Scientific and Industrial Research Organization, CSIRO Mineral Resources, Kensington, WA 6151, Australia*
[4] *Emergo s.r.l., Cascina, 56021, Italy*

Accepted 2025 December 4. Received 2025 December 3; in original form 2025 April 16

SUMMARY

Induced polarization (IP) effects in airborne electromagnetic (AEM) surveys have commonly been investigated in helicopter-borne systems, leaving both a bibliographic and application gap for fixed-wing configurations. This gap partly reflects the large relative number of helicopter compared to fixed wing AEM systems, but also the geometric complexity of fixed wing platforms. In these platforms, nine geometric parameters come into play: the pitch, roll and yaw of both transmitter and receiver, plus the three-axis offsets between the coils. Shifts in these factors can distort the measured data in ways that are not uniquely attributable, making it hard to pinpoint whether negative recordings truly arise from IP or from geometry-related effects. The non-fixed geometry also complicates removal of the primary field, often requiring iterative processing steps that may suppress or alter spectral content linked to IP. With advances in airborne IP understanding from helicopter-borne systems, revisiting fixed-wing platforms is both timely and necessary. Part A of this two-part study addresses this issue using the TEMPEST™ fixed-wing system connecting numerical modelling with field evidence. A suite of synthetic two-layer models with variable resistivity and chargeability parameters was developed to evaluate the system's sensitivity to polarizable structures. The experiments demonstrate that IP effects, including negative secondary field responses, can be reliably detected in fixed-wing AEM data, both in X and Z magnetic field components. The capacity of these systems to detect IP phenomena is, however, strongly dependent on the electrical conductance of the environment. For instance, both fixed-wing and helicopter-borne systems, elevated near-surface conductance enhances the amplitude of purely electromagnetic induction currents, which in turn can dominate the recorded response and obscure the comparatively weaker polarization currents. More in general, IP detectability depends on the strength of the EM response generated by induction currents flowing elsewhere, which can dominate the small reverse current flow from a polarizable target. This highlights the critical role of near-surface conductivity in controlling the expression of IP responses and underscores the need to carefully account for these factors when interpreting survey data. The synthetic results are then connected with field-scale observations from a subset of the AusAEM data set, over 470 000 line-km of TEMPEST™ data, where negative responses align with areas of low shallow conductance, confirming the simulation results. These finding open the way to the Part B of this study, where TEMPEST™ data are inverted taking into account IP and compared with helicopter-borne results and geological information.

Key words: Electrical Properties; Australia; Electromagnetic theory; Induced Polarization.

INTRODUCTION

Airborne electromagnetic (AEM) data are sensitive to the frequency-dependence of the ground conductivity, that is, to the induced polarization (IP) effects when acquired over a chargeable ground. This phenomenon, also referred as Airborne Induced Polarization (AIP), was theoretically discussed by Spies (1974, 1980); Lee (1981) and Flis (1987), with Smith & Klein (1996) being the first to demonstrate the presence of IP effects in Airborne fixed-wing EM data. Since then, many authors (e.g. Marchant *et al.* 2014; Macnae 2016a,b and 2016c; Viezzoli *et al.* 2017) have extended the understanding of the physics involved and its relationship with geology. AIP effects manifest in the EM data with typical signatures such as negative voltages and/or 'steep decays' (i.e. signals that decay faster than the typical $t^{-3/2}$ rate for the B field) of the recorded transients (e.g. Viezzoli & Manca 2019). The negative records are easily recognizable in the dataspace and are uniquely relatable to ground polarization when data are acquired with concentric-loop systems (Gubatyenko & Tikshayev 1979; Weidelt 1982). For a Slingram configuration, as in the case of fixed-wing AEM systems, negative voltages may also be consequence of the transmitter-receiver separation, complicating AIP recognition in the data space, as well as of the receiver orientation.

The importance of modelling IP effects from AEM data has been demonstrated, among others, by Macnae *et al.* (2016a), Viezzoli *et al.* (2017) and Lin *et al.* (2019). The authors showed how inaccurate conductivity models are derived when capacitive effects are overlooked during inversion. Examples from literature include incorrect estimates of the depth of conductive features (Kaminski & Viezzoli 2017), poor estimates of cover thickness (typically overestimated in the non-IP inverted models) (Viezzoli & Manca 2019) and a reduction in the depth of investigation for retrieved conductivity models (Viezzoli *et al.* 2021; Viezzoli 2023). At the same time, using a dispersive-resistivity model (such as the Cole & Cole model) to invert EM data makes the inverse problem strongly ill-posed expanding the model space to potential equivalent solutions. Moreover, when the measured data do not show negative responses, the IP effects are even more subtle and inverting to solve the ground polarization requires a highly accurate EM system description (in terms of injected current, system geometry, waveform, flight altitude etc) to avoid the introduction of further ambiguities.

Primarily for these reasons, most studies on airborne IP modelling have been carried for data acquired using concentric loop helicopter-borne platforms (see e.g. Macnae *et al.* 2016a,b,c; Hine and Macnae 2016; Viezzoli & Manca 2019). The unique relationship between negatives and AIP, and the accuracy with which it is possible to describe the geometry of these systems has made helicopter-borne platforms more suitable for AIP investigation. In contrast, extensive analysis on the fixed-wing systems sensitivity to AIP effects has never been published. The geometry of these systems, with a high number of degrees of freedom (transmitter and receiver pitch, roll, yaw and bird position), resulting in a high degree of non-uniqueness between data and IP effects has discouraged analysis of fixed-wing EM data considering polarization effects. Variability between the horizontal and vertical separation of the transmitter and receiver bird does not allow an unambiguous relationship between negative recordings and IP effects, as well as introducing potential inaccuracies for system response and primary field removal routines which require a correct geometrical description (Lane *et al.* 2000). In this sense, additional complexities arise also from the complex processing steps that are employed in the treatment of data acquired with these platforms. This can include deconvolution and re-convolution to B field data, as presented by Lane *et al.* (2000), data-replacement with exponential fitting and frequency-domain filtering that could bring to a possible spectral depletion of IP content in the delivered data. In addition, as for helicopter-systems, IP effects in fixed-wing EM data are often weak and can be obscured by the total EM response. Therefore, they can be difficult to detect and differentiate from noise, lack of signal in restive areas and 2-D or 3-D effects within the system footprint.

Recent developments in the processing of fixed-wing data (see e.g. Ley-Cooper & Brodie 2013; Brodie *et al.* 2019), in modelling approaches (see e.g. Fiandaca *et al.* 2024; Ray 2021), the understanding of AIP (Dauti *et al.* 2023) and in the system control of fixed-wing systems (Mulè & Smiarowski 2013), has allowed a re-think on the fixed-wing AEM capabilities in AIP detection and modelling. Fixed-wing AEM systems are increasingly being used in the mapping of large areas, with associated cost-benefits, and data acquisition rates (see e.g. Ley Cooper 2019; Minsley *et al.* 2021). The AusAEM project (Ley Cooper *et al*., 2019), constituting the first continental scale airborne EM survey being conducted to map the ground resistivity of the entire Australian continent, represents an example of where fixed-wing systems are being used extensively. Besides being able to model the regional scale resistivity of the country, the opportunity presents to being able to model the AIP from these data sets adding a significant additional layer of information for geological mapping. Consideration of AIP in this context may also aid the generation of more accurate resistivity models. Imaging IP processes from fixed-wing and heliborne EM data opens the way for comparisons with ground-IP measurements, which may bring a shift in the way the AEM data are used and interpreted at large scales. In this paper we aim to extend our understanding of fixed-wing AEM system capabilities in AIP detection and modelling, focusing on the analysis of data from the TEMPEST™ fixed-wing time domain system (Lane *et al.* 2000).This study on AIP responses in the TEMPEST™ system is structured in two parts, designated A and B. Part A is dedicated to connect the sensitivity analysis to IP of the TEMPEST™ system on synthetic models to field data (i.e. negative recordings in relation to near-surface geology) using the entire TEMPEST™ AusEM data set flown over the Australian Continent (Ley Cooper *et al*., 2019), whereas Part B addresses the inversion of field data incorporating IP effects. In both parts, comparative assessments with the SkyTEM^{312} FAST system are undertaken, through sensitivity analyses in Part A and inversion evaluations in Part B.

DATA MODELLING: THE FORWARD ALGORITHM

The TEMPEST™ and SkyTEM^{312} FAST forward responses have been computed following using the EEMverter modelling algorithm proposed by Fiandaca *et al.* (2024). The 1-D forward modelling accounts for the receiver's filter characteristics, the transmitter geometry and the source waveform. Following the classical formulation of Ward & Hohmann (1988), the EM response is computed in the frequency domain (FD) where the transmitter is modelled as a vertical magnetic dipole $m\boldsymbol{u}_z$ (where $\boldsymbol{u}_z$ is the versor along the z axis and m is the dipole moment) located at $-h$ metres above the surface of the Earth. For a N-layer 1-D model described in terms of complex conductivity $\boldsymbol{\sigma^*} = \{\sigma^*{}_1, \ldots, \sigma^*{}_N\}$ and layer thicknesses $\boldsymbol{thk} = \{thk_1, \ldots, thk_{N-1}\}$, the magnetic field is computed for both vertical (H_z) and radial (H_ρ) components as a function of angular frequency ω, receiver elevation $-z$ and distance between receiver and transmitter $\rho = \sqrt{x^2 + y^2}$ as:

$$H_z\left(\boldsymbol{\sigma}^*, \boldsymbol{thk}, \omega, \rho\right) = \frac{m}{4\pi}\int_0^\infty \left[e^{-u_0(z+h)} + r_{TE}e^{u_0(z-h)}\right]\frac{\lambda^3}{u_0}J_0(\lambda\rho)\,\mathrm{d}\lambda \tag{1}$$

$$H_\rho\left(\boldsymbol{\sigma}^*, \boldsymbol{thk}, \omega, \rho\right) = \frac{m}{4\pi}\int_0^\infty \left[e^{-u_0(z+h)} + r_{TE}e^{u_0(z-h)}\right]\lambda^2 J_1(\lambda\rho)\,\mathrm{d}\lambda, \tag{2}$$

In equations, J represents the Bessel function (J_1 of order 1 and J_0 of order 0), $u_0 = \sqrt{\lambda^2 - \omega^2\mu_0\varepsilon_0}$ and r_{TE} represents the reflection coefficient of the electric field transverse to the z axis, defined as:

$$r_{TE} = \frac{Y_0 - \hat{Y}_1}{Y_0 + \hat{Y}_1}, \tag{3}$$

where the intrinsic admittance of the free space Y_0 and the surface admittance $\hat{Y}_1$ are computed using the relations:

$$\hat{Y}_n = Y_n \frac{\hat{Y}_{n+1} + Y_n \cdot \tanh\left(u_n thk_n\right)}{Y_n + \hat{Y}_{n+1} \cdot \tanh\left(u_n thk_n\right)} \tag{4}$$

With:

$$Y_n = \frac{u_n}{\hat{z}_n} \tag{4a}$$

$$\hat{y}_n = \sigma_n{}^*(\omega) + i\varepsilon_n\omega \tag{4b}$$

$$\hat{z}_n = i\mu_n\omega \tag{4c}$$

$$u_n = \sqrt{\lambda^2 - k_n{}^2} \tag{4d}$$

$$k_n{}^2 = -\hat{y}_n\hat{z}_n \tag{4e}$$

$$\hat{Y}_N = Y_N \tag{4f}$$

The computation of $\hat{Y}_1$ is performed iteratively, starting from the last layer N. In all equations no variations in dielectric permittivity and magnetic permeability are assumed among layers (i.e. $\varepsilon_n = \varepsilon_0$ and $\mu_n = \mu_0$). In eq. (4b), the complex conductivity is expressed as re-parametrization of the Cole & Cole dispersive-conductivity model through maximum phase angle (MPA), as proposed by Fiandaca *et al.* (2018).

For the TEMPEST^{TM} system, the step response is computed as time-transform through Hankel transform of the FD kernel of eqs (1) and (2) (divided by $i\omega$). For the impulse response, we follow the approach from Fitterman and Anderson (1987), convolving the $\partial B/\partial t$ response with the current waveform for piecewise linear current waveforms.

SYNTHETIC SENSITIVITY STUDY

Methodology

In the following experiments, we aim to assess the capability of the TEMPEST^{TM} system to detect AIP effects and to resolve AIP parameters during inversion in a manner comparable to helicopter-borne systems. Evaluating both data space and model space is essential: the data space characterizes how AIP distortions manifest in the measured responses, whereas the model space quantifies the impact of these distortions on parameter resolution and trade-offs. Data-space analysis is conducted following the workflow proposed by Pitts *et al.* (2021) for the SPECTREM fixed-wing AEM system, while model-space investigation is performed through covariance matrix analysis, with results compared against analogous from the SkyTEM helicopter-borne system.

Table 1. Conversion between the Cole & Cole chargeability and MPA phase for time constant of 0.001 s and C of 0.5.

Cole & Cole chargeability (mV V^{-1})	MPA phase (φ) (mrad)
1.4	0.3
14.4	3
134.9	30
783.5	300

The dataspace inspection involves comparing forward responses computed from simple two-layer models, both with and without IP effects. For each pair of responses, a percentage difference is calculated to quantify the distortions introduced by chargeability relative to the non-IP response (assuming identical resistivity values and vertical discretization). In total, ∼400 000 forward responses are generated across different model parametrizations, and the resulting distortions are visualized as 2-D maps, with two parameters varying along the axes (e.g. resistivity versus phase or resistivity versus first-layer thickness). The workflow is summarized in the three points below:

(1). Define two synthetic models (*a* and *b*), parametrized with:

- a shallow first layer with a dispersive resistivity (ρ, φ, τ_φ, c, thk) over a purely resistive (non-dispersive) layer.
- a shallow first layer with non-dispersive resistivity (ρ, thk) over a purely resistive (non-dispersive) layer. For this non-IP-affected model, we use the same layer thickness and zero-frequency resistivity as for the IP-effected model (*a*).

As dispersive-resistivity model, the maximum phase angle (MPA) re-parametrization of the Cole & Cole model proposed by Fiandaca *et al.* (2018) has been used. Here, the model space is described as $\{\rho, \varphi, \tau_\varphi, C\}$, where the maximum phase φ of the complex conductivity (i.e. minimum phase of complex resistivity changed of sign) is used instead of the classic Pelton chargeability m_0 (Pelton *et al.* 1978), and the relaxation time τ_φ is defined as the inverse of the frequency (angular) at which the maximum phase is reached. With this parametrization, as shown by Fiandaca *et al.* (2018), the parameter correlations are decreased, particularly between the parameters φ and C as compared with the classic m_0 and C parameters. However, Fiandaca *et al.* (2018) investigate only the Cole-Cole re-parametrizations from an inversion point of view, without any claim on the petrophysical link between parameters and IP mechanisms. In this regard, it is worth to note that the MPA time constant τ_φ, even though it is a good inversion parameter, it is not necessarily to best one in terms of link to mineralization properties, as shown recently by Macnae (2025), which suggests that the time constant τ_σ *of* the conductivity Cole-Cole model is linked more directly to blocked/free conduction paths in mineralized media.

In Table 1 the correspondence between the Cole & Cole chargeability and the MPA maximum phase is presented. The relation between the two depends also on the relaxation time and the frequency exponent of the Cole-Cole model, and the presented conversion is computed for a time constant (τ_φ) of 0.001 s and a frequency dependence (C) of 0.5.

(2). Compute the 1-D forward response for both the models.

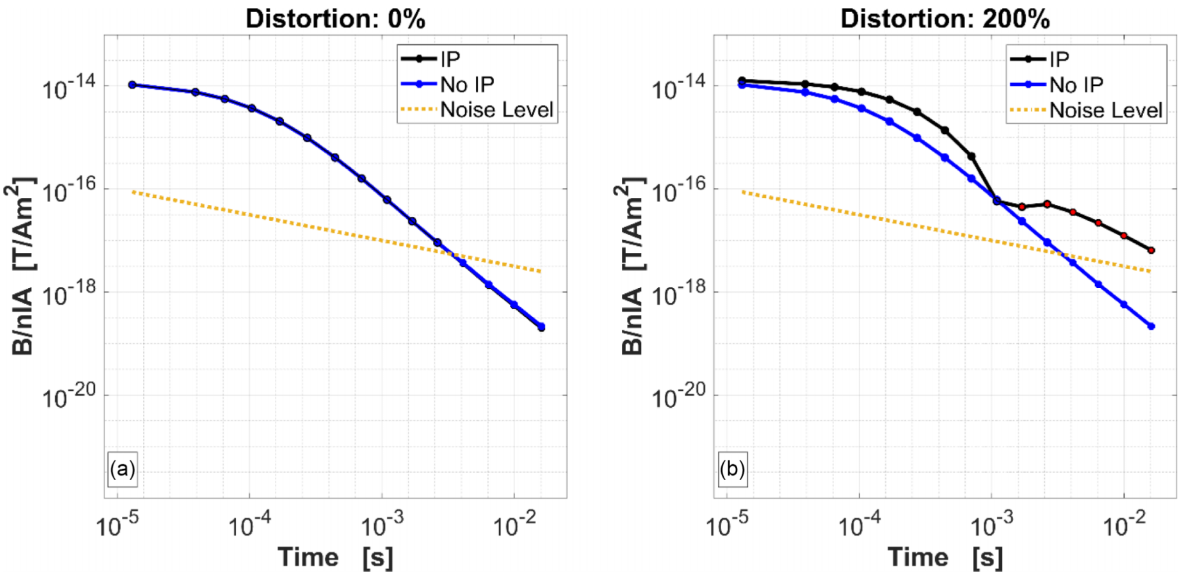

Figure 1. Examples of distortion produced by different amounts of chargeability for a homogeneous medium. In both figures, the blue curve shows an Airborne EM transient unaffected by IP effects, in black its equivalent computed for a chargeable medium and in yellow the noise level. The distortion above noise level (eq. 5) produced by the chargeable ground is indicated in the title.

(3). Compute the percentage difference between the forward responses, as in eq. (5):

$$\text{Distortion}_i = \sum_{j=1}^{n} \frac{100}{n} \left| \frac{fwr_{\text{NOIP}\,j} - fwr_{IP\,j}}{fwr_{\text{NOIP}\,j}} \right|, \quad (5)$$

where fwr_{NOIP} indicates the forward response computed for the non-polarizable model while fwr_{IP} is the forward response computed for the chargeable model. The subscript j refers to the gate number that goes from 1 to n (i.e. the number of gates above the noise level). The percentage difference is computed for the gates whose difference (between the AIP and non-AIP forward responses) is higher than the noise level to quantify the detectable distortions only. A simple noise model has been used, with level set at $10^{-17.5}$ T Am^{-2} at 0.001 s and decreasing in time as $t^{-\frac{1}{2}}$, a value compatible with the TEMPEST™ noise measured in the AusAEM project (Ley Cooper *et al.*, 2019). It is worth to note that this noise model is not simply a sensor noise level, because the signal is not measured directly as a square-wave B field, but the cumulative effect of the noise in the acquisition system and the uncertainty linked to pre-processing data manipulation (deconvolution of system response; primary-field removal; conversion to square-wave magnetic field).

With this approach we assume that all the distortions we measure can be attributable to IP effects only. Two examples of comparison between a purely resistive and polarizable models forward responses for the TEMPEST™ Z component are represented in Fig. 1.

In Figs 1(a) and (b), the forward responses are computed for a conductive (25 Ω m) first layer of 30 m of thickness over a resistive second layer. In blue, the forward response for the purely resistive medium is plotted, and for the polarizable medium it is plotted in black. On the lefthand side (Fig. 1a) the AIP forward response is computed for a weakly polarizable first layer ($\varphi = 0.2$ mrad, $\tau_\varphi = 0.001$ s, C = 0.2, corresponding to 3 mV V^{-1}), while on the righthand side (Fig. 1b) the response for a strongly polarizable first layer ($\varphi = 115$ mrad, $\tau_\varphi = 0.001$ s, C = 0.2, corresponding to 780 mV V^{-1}) is shown. In each plot (Figs 1a and b), the AIP negative gates are represented in red, and the system noise level is represented by the yellow dashed line. The large dots shown in each plot represent the time windows over which the mean percentage distortion is computed, that is, where both the forward responses are above the noise level. The value of the percentage distortion is shown above the plot. The results indicate that, as expected, increasing the chargeability of the first layer increases the distortion.

Table 2. Parameter range used to compute the forward responses. The "number of values" specifies how many points, between the minimum and maximum, are used to sample the model space for that parameter.

Parameter	Minimum value	Maximum value	Number of values
Resistivity (Ω m)	1	1000	35
Phase (mrad)	0.2	300	35
C	0.1	0.9	3
Time constant (s)	1e-05	1	5
First layer thickness (m)	5	100	10

The workflow was repeated for ∼400k forward responses, for both the X and the Z components. The models are defined with a two-layer configuration. Here, the shallow layer parametrization varies with each workflow cycle (repetition of point 1, 2 and 3), while the deeper layer is kept constant as a purely resistive layer. Although only the shallow layer can be chargeable, this assumption permits a reduction in the model-space ambiguities, thereby allowing us to better link the AIP distortions with meaningful geological models. From a geological perspective, the deep layer is representative of a resistive basement, while the layer above can represent a range of geological settings ranging from outcropping basement to thick cover. The parametric ranges for which we computed the forward responses are listed in Table 2:

The ranges of the parameter values represent possible geological scenarios. The phase range has been selected considering both electrode and pore/grain polarization mechanisms: phase values up to several hundreds of milliradians are typical for mineral polarization

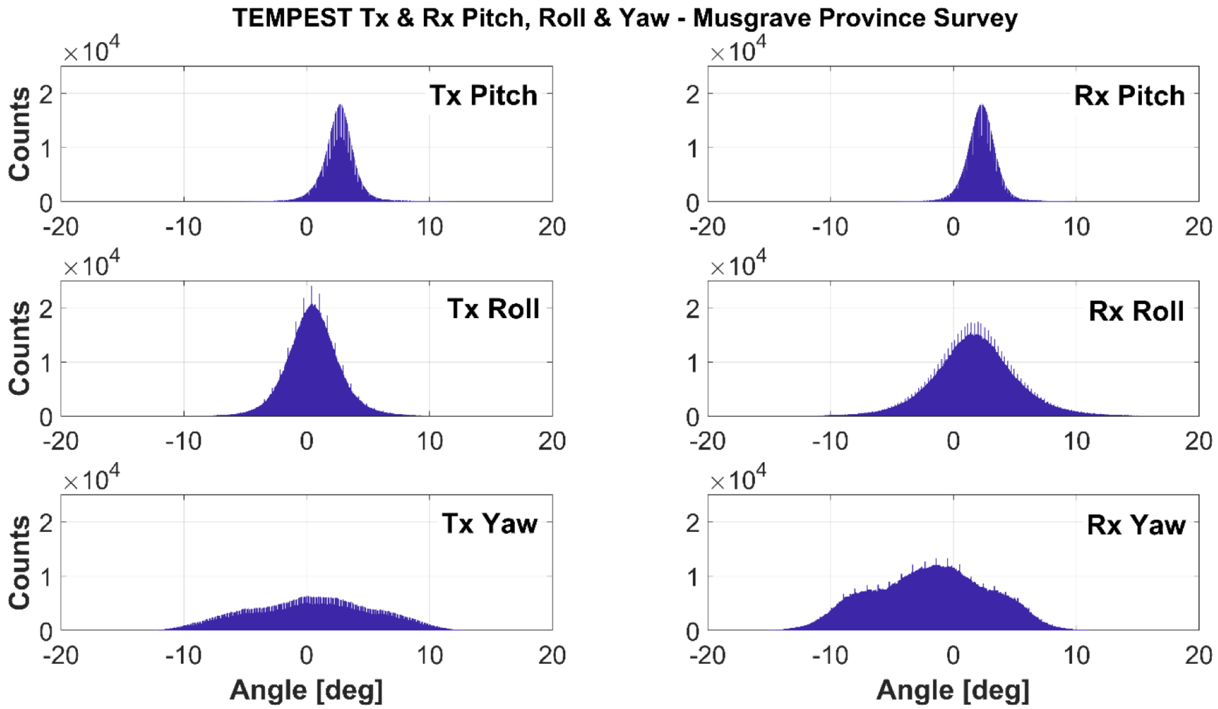

Figure 2. Recorded transmitter and receiver pitch, roll and yaw for TEMPEST^{TM} AEM data acquired over the Musgrave Province in South Australia. The collected recordings are from a survey of approximately 20000 line kilometres.

(e.g. Pelton *et al.* 1978), while polarization in sedimentary materials can reach phase values up to a few tens of milliradians, considering a linear relation between surface polarization and surface conduction as in Weller *et al.* (2013). The time constant is related to the grain size of the chargeable particle and, increasing the grain size, typically the time constant increases and the chargeability decreases (Pelton *et al.* 1978; Martin & Weller 2023). Regarding the frequency dependence, a value of $C = 0.5$ corresponds to a Warburg case polarization while, when C tends to 0, to a Constant Phase Angle configuration (e.g. Van Voorhis *et al.* 1973). When the frequency dependence C is small, the time constant is less resolved given the wide spectral range covered by the chargeability frequency peak. For glacial environments, a frequency dependence higher than 0.8 is necessary to fit the data together with time constants lower than 10^{-05} s (e.g. Lorentzen *et al.* 2024). For sedimentary materials, such as clay and sands, the spectral behaviour is strongly related to the water content (e.g. Breede *et al.* 2012), the effective pores and the effective area of the geologic material. More in general, the clay minerals show a high chargeability, given their larger specific surface area, and increase the total chargeability in sand-clay mixtures. With the proposed parametrization we can span from a conductive cover over a resistive basement (representative of a typical Australian setting), to a chargeable resistive shallow layer that can represent an outcrop without cover. It is important to note that AEM systems, are considered sensitive to high-frequency polarizations (given the limits in the system base frequency) and to strong chargeability only (Macnae *et al.* 2016b). In geological terms, this means sensitivity to non-economic minerals, clays and fined grain materials. With this set of experiments, we also aim to verify whether for high time constants (of 1 s) and low chargeability, fixed-wing EM systems have sensitivity to IP effects.

For the computation of the forward responses, the TEMPEST^{TM} system geometry is described as:

- Tx–Rx horizontal distance: 100 m
- Tx–Rx vertical distance: 50 m
- Tx altitude: 120 m
- Rx and Tx Pitch: 0°
- Rx and Tx Yaw: 0°
- Rx and Tx Roll: 0°

For the purposes of the simulation, selection of zero values for pitch/roll and yaw was determined from an assessment of all recorded attitude values for a TEMPEST^{TM} survey conducted as part of the AusAEM project flown over the Musgrave Province in central Australia, as well as from the analysis of the effect of the attitude angles on the forward response.

The analysis of the measured attitude values was made possible by the instrumental improvements resulting by the extensive use of the TEMPEST^{TM} system, including the monitoring and active measurement of the system geometries during the acquisition (e.g. Mulè & Smiarowski 2013; Brodie *et al.* 2019). This provides fundamental information for the TEMPEST^{TM} modelling, helping reduce potential ambiguities during inversion.

The attitude angles measured in the Musgrave survey, covering approximately 20 k line-km, are shown in Fig. 2, while the mean and standard deviation values for the pitch, roll and yaw distribution are shown in Table 3. All the mean attitude angles fall within one standard deviation from zero degree. However, a small deviation from zero of the receiver pitch has significant consequences on the TEMPEST^{TM} data, as shown in Fig. 3 for a purely resistive two-layers model. The forward responses are computed with a first layer

Table 3. Mean and standard deviation of recorded pitch, roll, and yaw for Musgrave Province infill flights from the AusAEM survey.

	Mean (degree)	Standard deviation (degree)
Tx Pitch	2.6	1.5
Tx Roll	0	2
Tx Yaw	0	5
Rx Pitch	2	2
Rx Roll	2	4
Rx Yaw	- 2	5

resistivity of 50 Ω m and a thickness of 50 m above an infinite-thick 1000 Ω m layer, varying both the receiver pitch and roll. In Figs 2 and 3, X and Z components are in the reference frame of the sensor, with pitch and roll defined as Tait-Bryan nautical angles.

Table 3 indicates the mean and standard deviation of the pitch, roll and yaw distributions of Fig. 2.

In Fig. 3 the simulated X component shows a late-time sign change with increasing pitch values, similar in shape to IP responses. Differently, the Z component does not show with increasing pitch any spurious negative data that could be related to ground polarization and the roll does not trigger negative data in any component. For these reasons, in the following simulations we used 0° for receiver pitch, in order to avoid ambiguities in meaning of negative data that are only IP-related with zero pitch.

Systems description

The characteristics of the systems used in these studies are summarized in Table 4. The table presents the specifications of various TEMPEST™ system configurations, both used in Part A and Part B of this work, along with a description of the SkyTEM312FAST system, which is later used to compare model covariance matrices (and in Part B for modelling comparisons). For completeness, the TEMPEST™ 208 configuration is also included in table.

The TEMPEST™ data, despite being acquired by a d*B*/d*t* coil, are pre-processed by the data provider to remove the effects of both primary field and system response. This pre-processing consists of three main steps: deconvolution of system response; primary-field removal; conversion to square-wave magnetic (*B*) field response (Lane *et al.* 2000). This conversion to square-wave *B* field reconstructs the signal with time gates that span a time range wider than the measured d*B*/d*t* range, with first gate at 13 µs and last gate at 16.2 ms. For the TEMPEST™ forward responses, we used the STANDARD configuration with a suited noise model. In particular,

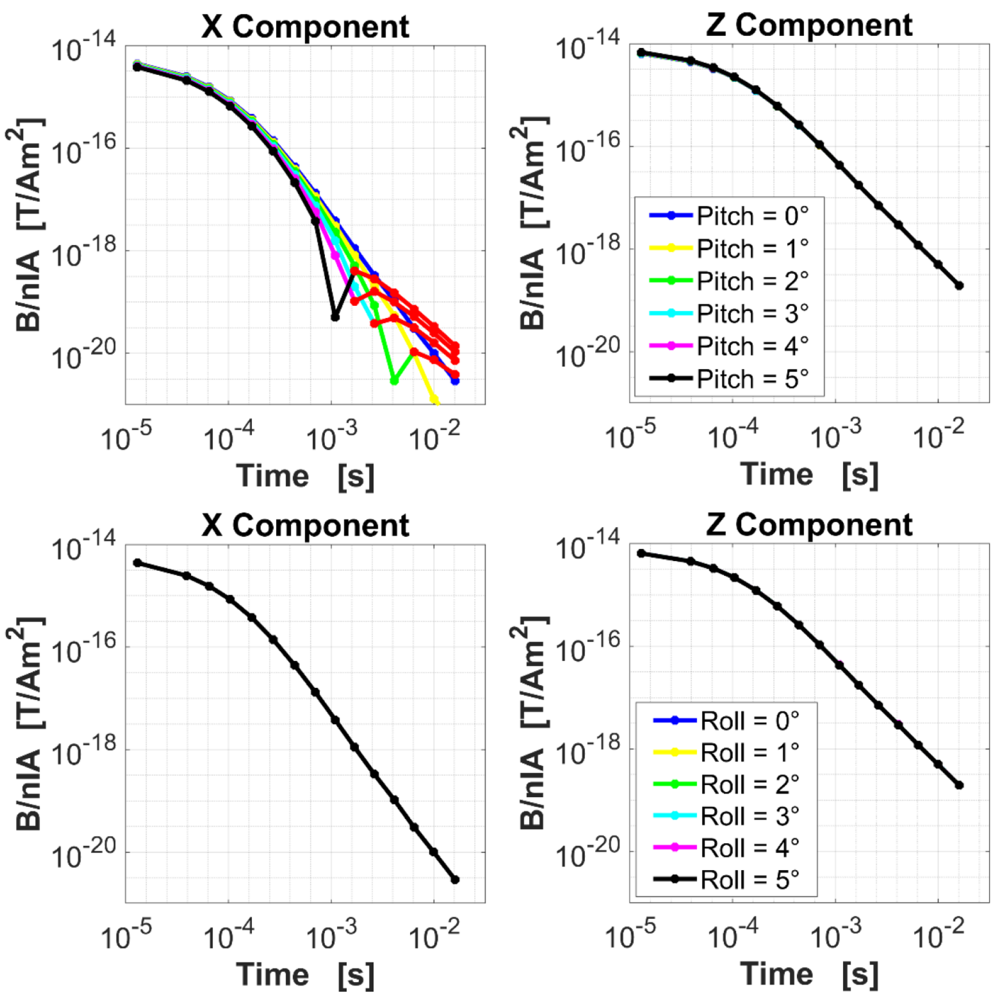

Figure 3. Examples of forward responses varying the receiver pitch (top) and roll (bottom) for the TEMPEST™ system. The responses are computed for a two-layers model, with a first layer resistivity of 50 Ω m and a thickness of 50 m. The second layer has an infinite thickness and a resistivity of 1000 Ω m.

Table 4. Summary of the features of TEMPEST™ and SkyTEM^{312}FAST system configurations.

	TEMPEST™ STANDARD	TEMPEST™ HIGH MOMENT	TEMPEST™ 208	SkyTEM^{312}FAST
Base frequency (Hz)	25	25	25	275 (LM) 25 (HM)
Transmitter area (m^2)	244	244	154	342 (LM and HM)
Transmitter turns	1	1	1	2 (LM) 12 (HM)
Waveform	Square	Square	Square	Pseudo-rectangular
Duty cycle	50 per cent	50 per cent	50 per cent	44 per cent (LM) 25 per cent (HM)
Transmitter pulse width (ms)	10	10	10	0.8 (LM) 5 (HM)
Transmitter off-time (ms)	10	10	10	1.018 (LM) 15 (HM)
Transmitter turnoff (µs)	42	80	∼ 55	2.5 (LM) 5–10 (HM)
Peak current (A)	280	1200	560	9 (LM) 120 (HM)
Number of transmitter turns	1	1	1	2 (LM) 12(HM)
Peak moment (Am^2)	68 320	292 800	86 240	6156 (LM) 492.480 (HM)
System bandwidth	25 Hz to 37.5 kHz	25 Hz to 37.5 kHz	25 Hz to 38.4 kHz	25 Hz to 300 kHz
Nominal Flying Height (m)	120	120	100–120	40–60
EM sensor	Towed bird -3 component d*B*/d*t* coils	Towed bird–3 component d*B*/d*t* coils	Towed bird–3 component d*B*/d*t* coils	3 component dB/dt coil
Nominal Tx-Rx horizontal separation (m)	117	117	115	13.5
Nominal Tx-Rx vertical separation (m)	41.5	41.5	45	0
Number of output windows	15	15	15	18 (LM) 17 (HM)
Window centre times (for TEMPEST™ after conversion to square-wave magnetic *B* field)	13 µs to 16.2 ms	13 µs to 16.2 ms	13.3 µs to 16.2 ms	16.41 µs to 0.861 ms (LM) 436.41 µs to 13.18 (HM)

a simple noise model has been used, with level set at $10^{-17.5}$ T at 0.001 s and decreasing in time as $t^{-\frac{1}{2}}$ (Ley Cooper *et al.*, 2019). For the SkyTEM system, to compute the data covariance matrices, a noise floor at 10^{-9} V Am^{-2} at 0.001 s has been used, typical for this system configuration.

Results of sensitivity study

To summarize the results (point 3 of the workflow), the computed percentage differences are plotted in a 2-D space (Fig. 4).

Given the number of model parameters, three were fixed while two were allowed to vary on the axis. The distortion value is higher than 0 where there is sensitivity to AIP, and it can span up to the 100 per cent where all the gates are distorted with a detectable AIP signature. Given that the AEM data are typically fitted within a few per cent of the recorded value (2 per cent–3 per cent), it is possible to assume that a distortion approximately higher than the 5 per cent can be enough to produce an artefact if the AIP affected data is modelled with a non-dispersive resistivity. Where at least one negative gate is recorded in the IP-related forward response, it is displayed with a black dot. These negatives can only be produced by IP effects and not by the geometry (considering the typical AusAEM values for pitch/roll/yaw and tx-rx distance—see Fig. 2). The results are here shown both for the Z and X component of the *B*- field forward response.

The computed percentage differences are here referred to a two-layer model; the shallower layer is parametrized with 50 m of thickness, a time constant of 0.001 s and a frequency dependence of 0.6. The results show how and where the IP effects distort the signal varying the resistivity and chargeability of the first layer. Results shown in Fig. 4 show that for both the components, the forward responses are not significantly (more than 5 per cent) distorted by AIP where the shallow layer is weakly chargeable and very conductive or very resistive. For the very conductive domain (where the resistivity is lower than 30 Ω m), pure EM currents are strong enough to overcome the opposite sign polarization effect and avoid the generation of significant distortions. A similar behaviour is observed when the ground is very resistive (more than 500 Ω m) with signal falling into noise (as shown in Fig. 1a) and the AIP effect becoming undetectable. At the same time, for both the scenarios, increasing the shallow layer chargeability to around 10 mrad, which are reasonable values for fine-grain sediments, the IP effects become significant enough to generate artefacts if not modelled. As general trend the AIP distortions become more significant when the first layer resistivity increases, that is, where the purely EM currents get weaker, and shallow layer chargeability increases, and IP currents get stronger. This is illustrated in Fig. 4, where the first

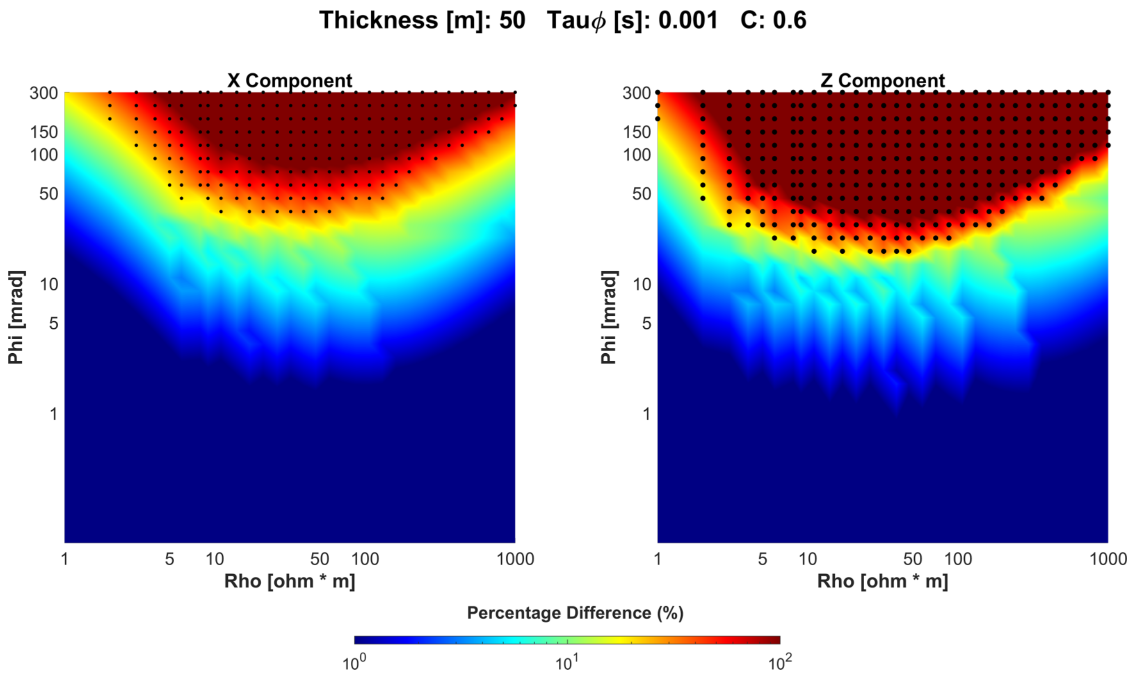

Figure 4. Representation of the amount of distortion produced by IP effects for a two-layer model with varying resistivity and chargeability of the first layer. The thickness, time constant and frequency dependence are fixed with values: thickness = 50 m, time constant = 0.001 s and $C = 0.6$. The colour bar indicates the degree of distortion expressed as a percentage following eq. (5). The distortion for the X component is shown on the left while that for the Z component is presented on the right. The black dots represent where negative voltages have been produced in the IP forward response.

layer is highly chargeable and the signal does not fall into noise. In this situation it is possible to detect negative voltages related to IP effects. These results are valid both for the Z and for the X component. The main differences between the two, for this set of experiments, lies in the negative voltage distribution that results in smaller chargeability values for the vertical component. In a very conductive domain, the Z component shows AIP distortions where the X doesn't (Fig. 4).

For the same set of models (thickness = 50 m, time constant = 0.001 s, $C = 0.6$, variable resistivity and phase), a comparative analysis of the model sensitivity of standard TEMPEST™ and SkyTEM^{312} FAST systems (Table 4) is also provided. The results of the analysis are shown in Fig. 5, where the relative uncertainty of the resistivity and phase parameters are shown for a two-layer model, varying the first layer properties (phase and resistivity). The parameter uncertainty is computed as the square root of the diagonal elements of the parameter covariance matrix C_m obtained, as proposed by Tarantola & Vallette (1982), propagating the data uncertainty through the Jacobian G:

$$C_m = \left[G^T C_d^{-1} G\right]^{-1}, \tag{6}$$

where C_d is the data covariance matrix.

The results of the sensitivity analysis are shown in Fig. 5.

As shown in fig. 5, the TEMPEST™ and SkyTEM312 systems exhibit comparable sensitivity values to both resistivity and chargeability. Model uncertainty increases with resistivity and remains high at low chargeability values. When only a single component of TEMPEST™ is analysed, sensitivity decreases at high resistivity; however, joint inversion of both components significantly expands the sensitivity range, making it largely comparable to that of SkyTEM312, and even slightly superior at higher resistivities for both resistivity and chargeability. Notably, the TEMPEST™ X component demonstrates greater sensitivity to ground polarization at high resistivities, consistent with the field data modelling results presented in Part B of this work. These results also indicate that, for a first layer of 50 m, a time constant of 0.001 s, and a frequency dependence of 0.6, ground polarization needs to exceed 10 mrad and be associated with a conductive near-surface (< 50 Ω m) to be reliably resolved by a single-component inversion (e.g. Australian altered cover). In contrast, when both TEMPEST™ components are jointly modelled, the inversion successfully resolves chargeability even in association with a resistive near surface (e.g. outcropping alteration or mineralization).

For a sensitivity analysis to IP parameters, it is also important to study the effect of the spectral parameters; the small time constant and the frequency dependence used Figs 4 and 5 describe a relatively fast polarization of the ground. As mentioned in the previous section (*'Methodology'*), other research has suggested (e.g. Macnae *et al.* 2016b) the limit beyond which it is no longer possible to measure AIP from airborne inductive EM platforms. Linked to this we present the results of an experiment where we increase the time constant of the shallow layer to 1 s (without changing all the other parameters), with results presented in Fig. 6.

A comparison of results from Figs 4 and 6 reveals that the parametric ranges over which distortions become detectable are broadly consistent across the two cases. Nevertheless, differences emerge in the reduction of negative voltage responses and the magnitude of the distortion. This behaviour depends on the relation between time-constant and the base frequency of TEM acquisitions. A high time constant in the Cole-Cole polarization shifts the maximum values of the phase/imaginary conductivity to lower frequencies, often preventing the effects of ground polarization from being recorded

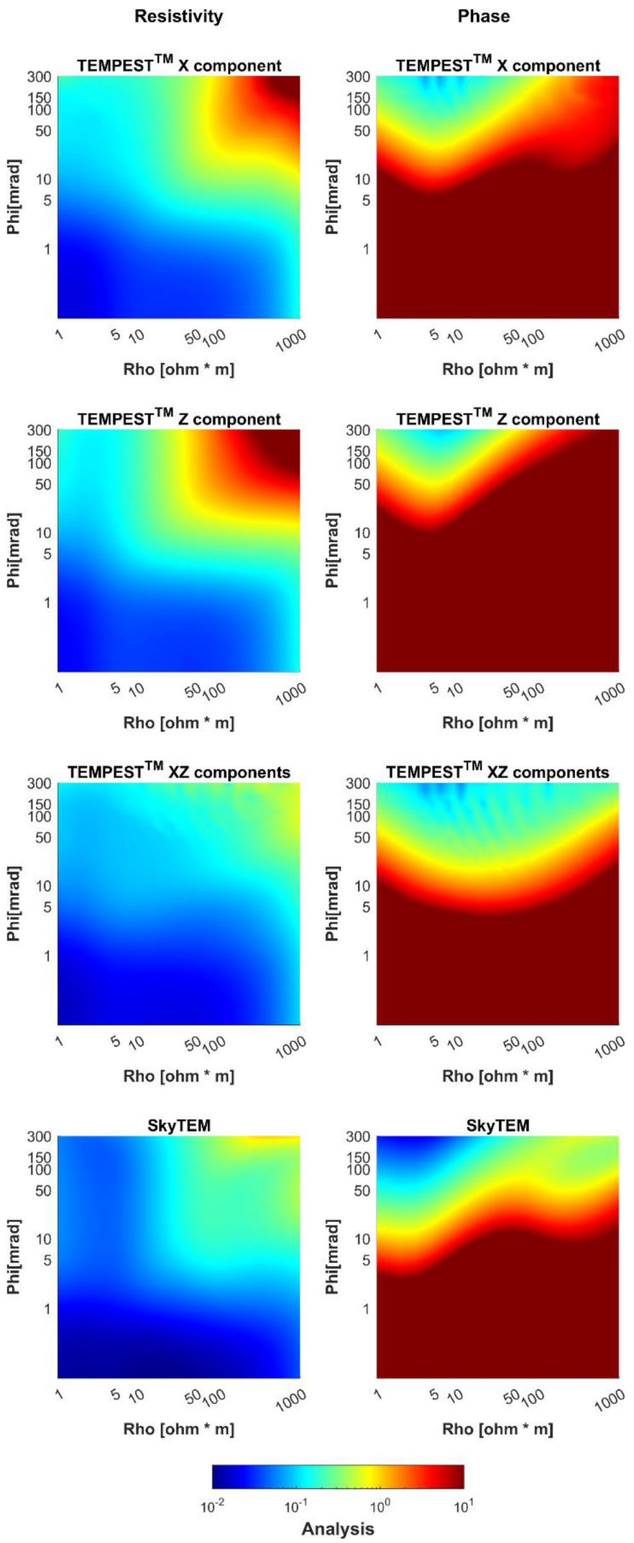

Figure 5. Relative uncertainty of resistivity (left) and phase (right) parameters for a two-layer model with varying resistivity and phase of the first layer. The thickness, time constant and frequency dependence are fixed with values: thickness = 50 m, time constant = 0.001 s and $C = 0.6$. The colour bar indicates the relative uncertainty of the parameters. From top to bottom: parameter uncertainty with X component of TEMPEST™ data; parameter uncertainty with Z component of TEMPEST™ data; parameter uncertainty with both X and Z component of TEMPEST™ data; parameter uncertainty with dual-moment SkyTEM^{312}FAST data.

with negative values within the AEM turn-off time. However, also with a 25 Hz base frequency substantial distortions can be recorded in presence of slow-polarization mechanisms (i.e. tau = 1 s). As a result, the distortions are present in data but may not be easily recognized in dataspace, leading to incorrect modelling if the AIP is not considered.

In Fig. 7 the effect of varying the first layer conductance $(thk \cdot \frac{1}{\rho})$ on AIP detection is shown. In contrast to the previous figures, the first layer resistivity and the thickness vary on the axis while chargeability, with smaller time constant (0.01 s), is maintained fixed for all the forward responses. For resistivity-thickness ranges illustrated in Fig. 7, the AIP is measurable, and a linear relationship is observed with the decrease of conductance (lowering in thickness or increasing in resistivity) is visible. In geological terms, the effects of an altered cover (chargeable and conductive) on the TEMPEST™ EM measurements are apparent. Assuming a cover resistivity between 1 and 20 Ω m, the thinner the cover, the stronger the AIP effects with negative voltages likely to be generated. Increasing the cover thickness accompanied by an increased conductance will limit the ability of polarization currents to overcome the EM eddy currents. Where the conductive cover is completely absent, results suggest that the signal fall into noise and AIP effects cannot be detected with these spectral characteristics. As with the other synthetic models, the AIP distortions are stronger for the Z than for the X component, a consequence of the offset between transmitter and receiver that does not allow the measurement of a change of sign in the horizontal component of the total magnetic field.

In summary the synthetic modelling studies suggest that the TEMPEST™ fixed-wing system is sensitive to AIP effects, both for the horizontal and vertical component. When a first layer over a resistive basement is polarizable, few milliradians (or $\mathrm{mV\,V^{-1}}$) of chargeability are enough to significatively distort the recorded data for a wide range of electrical parameters. Numerical simulations show that AIP distortion is absent only when the first layer is either highly conductive with low chargeability or very resistive such that the signal falls into the noise level. As illustrated in Fig. 5, the TEMPEST™ system resolves the ground chargeability in a comparable way with the SkyTEM^{312} system: for a first layer strongly chargeable (>50 mrad) and conductive, the ground polarization is well resolved. Geologically, this configuration can be representative of a thin cover setting. Importantly, AIP effects in TEMPEST™ data are not always evident through negative measurements. More commonly, they distort the recorded responses without producing obvious effects in dataspace. This complicates AIP recognition in dataspace and increases uncertainty during inversion. Nevertheless, ignoring these effects during modelling can lead to an inaccurate resistivity model.

VALIDATION ON FIELD DATA

To verify the synthetic results, the map of the negative voltages for part of the AusAEM TEMPEST™ data set, as flown in the period up to 2020, have been produced and compared with other available geophysical and geological national maps. The distribution of negatives has been produced only where there are more than 3 sequential negative records in the same transient which sit above the noise level (i.e. 10^{-17} T Am^{-2} at 0.001 s as described in the workflow). We have also neglected negative measurements in the first 2 gates, as these could be a consequence of a geometrical offset in conductive environments. We used the same noise level employed in the synthetic study for the negative mapping of the field data.

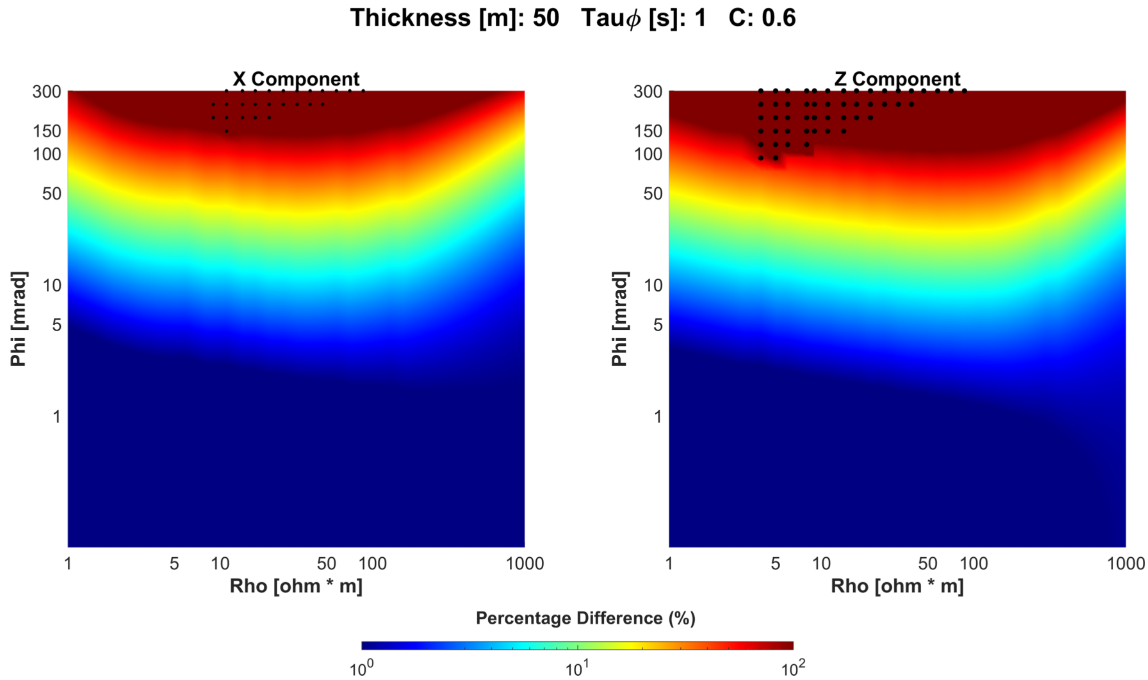

Figure 6. Distortion plot varying the first-layer resistivity and chargeability computed with a time constant of 1 s. The black dots represent where negative voltages have been produced in the IP forward response.

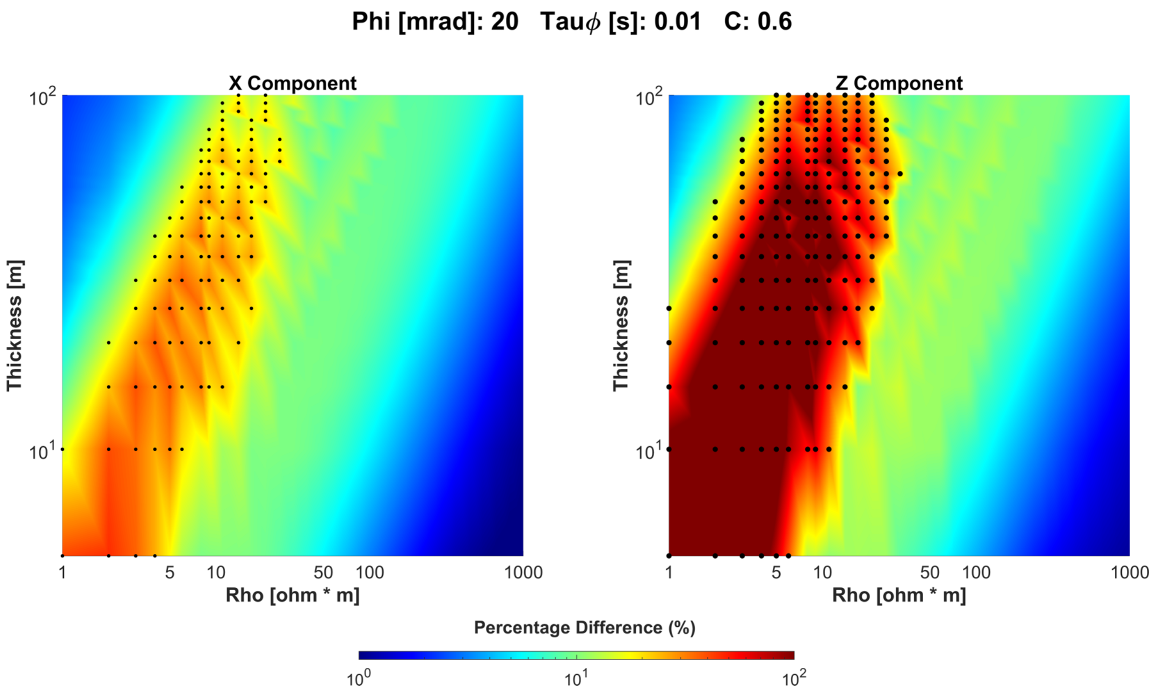

Figure 7. Distortion plot for a varying thickness-resistivity model. The other parameters are fixed (phi = 20 mrad, time constant = 0.01 s and $C = 0.6$). The graph shows the variation of distortion produced by AIP when varying the conductance of the first layer. The black dots represent conditions where negative voltages have been produced in the IP forward response.

The first comparison has been done with the Australian regolith thickness map produced by Geoscience Australia in 2015 (Wilford *et al.*, 2016) to prove the results shown in Figs 4, 6 and 7. The map is shown in Fig. 8.

Assuming a quick polarization ($\tau_\varphi < 0.01$ s) for the regolithic cover, a good spatial correlation between the area having a thinner cover and the negative measurements is shown as suggested would happen in the synthetic modelling (see Fig. 7). The correlation with

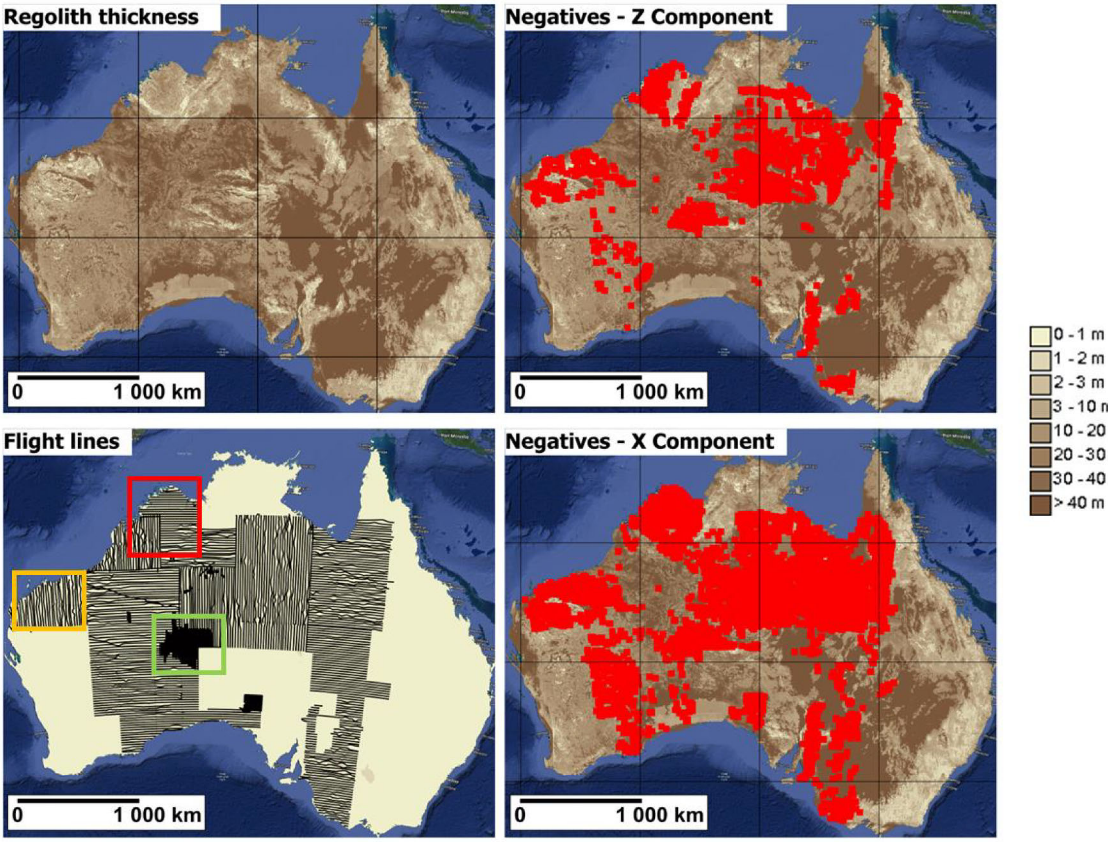

Figure 8. Map of negative voltages (red squares) over the cover thickness map for Australia. At top-left the depth of regolith map is shown while the AusAEM flight lines are shown at bottom-left. The map of negative recordings for the Z component is shown at top-right while for the X component at bottom-right. The colour bar indicates the regolith thickness value. In the map on the bottom left, the coloured squares indicate the regions of fig. 7: Kimberley in red, Pilbara in orange, Musgrave in green.

the geology of the Australian sub-continent is also apparent when comparing negatives with the lithological map shown in Fig. 9. Here results are presented for the NW of Australia, including the Pilbara (in North-West), Kimberley (North) and Musgrave (South-East) regions.

The surface geology depicted in the Australia Map (2012 edition) shows a good correlation between the negative distribution and the outcropping domains in map for all the three regions. There is also a correlation between areas of Mesoproterozoic metamorphic complexes in the Musgrave (in grey), and with the ultramafic Archean basalts (in green) in the Kimberley and Pilbara and with the Neoproterozoic sedimentary sequences in brown on the map. It is interesting to note that not all areas associated with sedimentary packages have coincident negative voltages. For instance, while in the Pilbara and Musgrave region there is a correspondence between the two, in the Kimberley and in the outcropping region between the Musgrave and the Kimberley the Proterozoic sediments give a poor negative response. This behaviour could be explained by the heterogeneity of the sedimentary body, comprising a mix of slightly metamorphosed mudstones, siltstones, conglomerates and breccias that can give a different physical response for different assemblages. Also, sediments can have very different conductivities (EM responses) which will change the IP effects. As well, the degree of weathering and whether thin transported regolith cover containing clays is present also affect the AIP response. Negatives associated with felsic magmatic bodies could be related to the presence of magnetite (Pittard & Bourne 2007) or disseminated sulphides in veinlet system that can give a polarizable response. At this scale, these correlations are suggestive, but they do provide an indication of where site-specific, finer-scale interpretation may warrant consideration of AIP effects.

In contrast to results from the synthetic modelling study, analysis of TEMPEST^{TM} data at the continental scale shows that the negatives are more frequently expressed in the X component of the B field than in the Z component. Here, the negatives can be consequence of a higher sensitivity of the X component to the 2-D effects that can produce negatives as well as variations in the receiver pitch during the flight. The X-component layered-Earth response exhibits a more rapid decay than the Z-component. This behaviour suggests that, at late delay times, the measurements are increasingly influenced by negative contributions arising from induced polarization return currents localized beneath the receiver. These return currents were energized during earlier delay times, when the induced current system remained proximal to the transmitter. However, the analysis of the AusEM data sets allows to connect the findings of the numerical modelling to the field evidence, with the thickness of the conductive cover driving the expression of negative TEMPEST^{TM} data. The natural continuation of this research is presented in the part B of this study, where TEMPEST^{TM} data are inverted, taking into account IP and comparing the results with coincident helicopter-borne EM derived models and geological information.

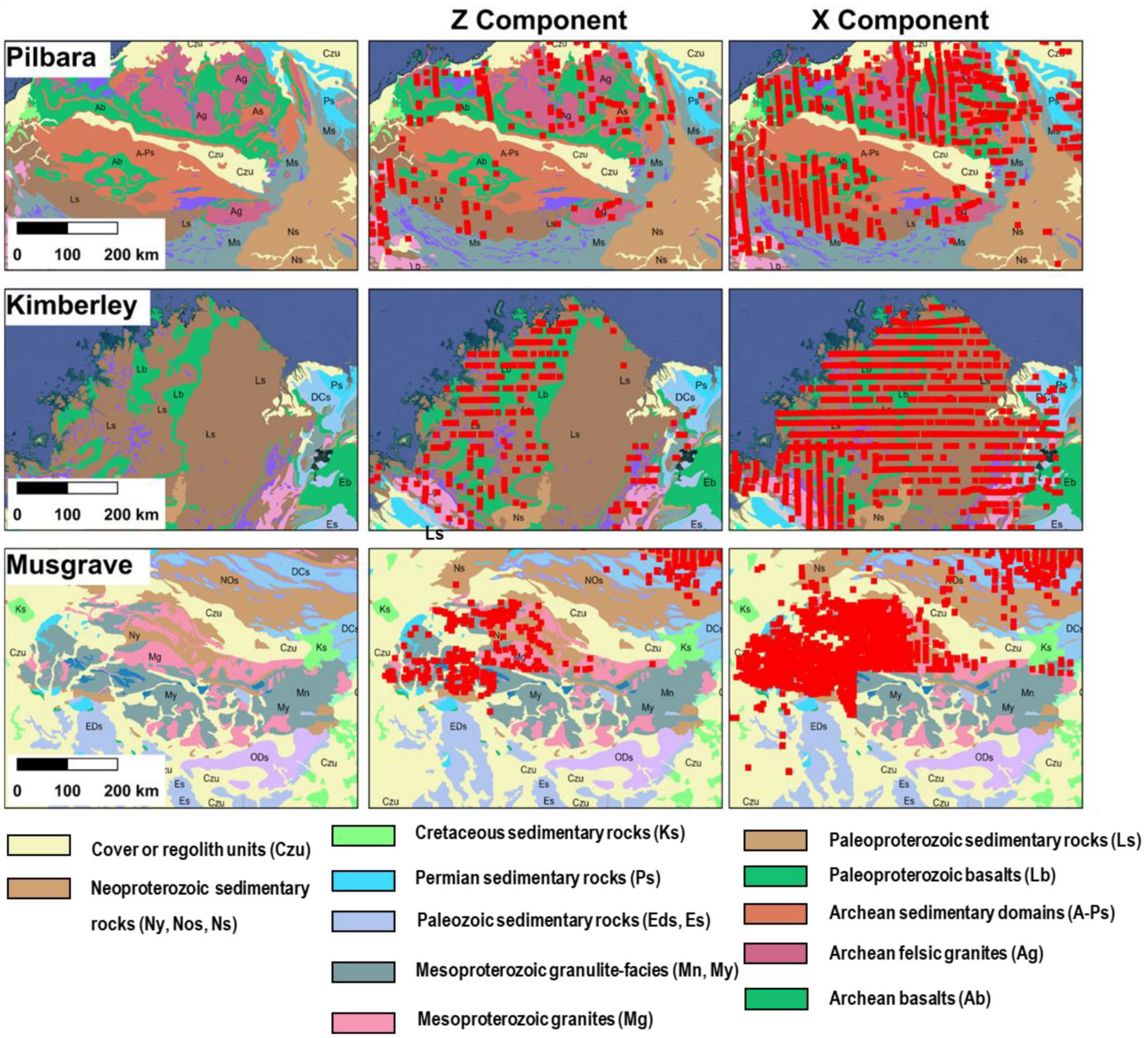

Figure 9. Detail of the map of correspondence between negative data (red squares) and surface geology. Pilbara (top), Kimberly (centre) and Musgrave (bottom) regions for Z and X components. Dark blue colour in Pilbara and Kimberley represent the ocean.

CONCLUSIONS

Part A of this series of study on airborne induced polarization (IP) using the TEMPEST^{TM} fixed-wing system demonstrates the system's sensitivity to IP effects. This conclusion is supported by synthetic forward modelling and continental-scale analysis of field data.

The result of synthetic modelling shows how AIP effects are detectable in TEMPEST^{TM} AEM data in a variety of geological scenarios. The AIP effects are likely to affect the TEMPEST^{TM} data predominantly when acquired in thin-cover or outcropping geological domains. In these settings, the IP currents develop into the ground and contrast with the fast-decaying purely EM currents giving measurable distortions of the recorded data. When the cover conductance is low, the IP currents dominate the EM currents and strong negative voltages can be measured. Alternatively, when the cover gets thicker or its conductivity is particularly high, the IP effects give negligible distortions in the recorded data, and it is possible to model the TEMPEST^{TM} with a non-dispersive resistivity model without retrieving artefacts, similarly to helicopter-borne systems. As a general observation, the synthetic study has shown how few milliradians of chargeability can result in significative distortions above the noise level. It is also important to highlight that IP effects can give measurable and significative distortions to AEM data even without negative responses in the dataspace. This behaviour has been also observed for the synthetic mapping with a high time constant (1 s), for which strong IP-related distortions are mapped with a reduced number of negative responses. A study of field data acquired by the TEMPEST^{TM} system within the entire AusAEM project confirms the synthetic results, highlighting the importance of geology on determining whether IP distortions can be detectable in TEMPEST^{TM} records. Thin regolithic cover and outcropping resistive geological bodies (such as granites rich in magnetite) control the distribution of negative recordings in field data sets. The geological control on the dataspace analysis shows encouraging possibilities in the modelling of AIP effects from the

TEMPEST™ system to map ground geology. The next phase of this study (Part B) on the TEMPEST™ fixed-wing system focuses on modelling field data, comparing inversions with helicopter-borne results and validating inverion models against a known mineralization.

ACKNOWLEDGMENTS

The work has been funded by the European Union SEMACRET project (Grant Agreement no. 101057741) and by the IPRaMa Project (Induced Polarization for Raw Materials Exploration).

We also acknowledge the reviewers of this paper, Prof. Jim Macnae and an anonymous Reviewer, for their thorough and very constructive reviews which greatly improved this paper.

DATA AVAILABILITY

The TEMPEST™ data acquired within the AusAEM project are publicly available from the Geoscience Australia portal (https://www.eftf.ga.gov.au/ausaem).

REFERENCES

Breede, K., Kemna, A., Esser, O., Zimmermann, E., Vereecken, H. & Huisman, J.A. 2012, Spectral induced polarization measurements on variably saturated sand-clay mixtures, *Near Surf. Geophys.,* **10,** 479–489.

Brodie, R.C., Ley-Cooper, Y., Lockwood, R. & Murray, D. 2019, AusAEM Year 1: some aspects of quality control and calibration, *ASEG Extended Abstracts,* **2019**(1), 1–5.

Dauti, F., Viezzoli, A. & Fiandaca, G. 2023, Joint Inversions of AEM modelling AIP effects: helicopter-borne, Ground IP and Fixed-Wing systems, in *AEM2023–8th International Airborne Electromagnetics Workshop, 3-7 September 2023,* Fitzroy Island, QLD, Australia.

Fiandaca, G., Chen, J. & Zhang, B. 2024, EEMverter, a New Modelling Tool for Electric and Electromagnetic Data with Focus on Induced Polarization, in *NSG 2024 30th European Meeting of Environmental and Engineering Geophysics, Vol. 2024,* European Association of Geoscientists and Engineers, Helsinki, Finland, pp. 1–5.

Fiandaca, G., Madsen, L.M. & Maurya, P.K. 2018, Re-parameterisations of the Cole–Cole model for improved spectral inversion of induced polarization data, *Near Surf. Geophys.,* **16,** 385–399.

Fitterman, D.V. & Anderson, W.L. 1987, Effect of transmitter turn-off time on transient soundings, *Geoexploration,* **24**(2), 131–146. ISSN 0016-7142..

Flis, M. 1987, IP Effects In 3-D Tem Data—Theory And Case Histories, *Explor. Geophys.,* **18**(1–2), 55–58.

Gubatyenko., V.P. & Tikshayev, V.V. 1979, On the variation of the sign of the electromotive force of induction in the transient electromagnetic field method, *Izv. Earth Physics.,* **15,** 217–219.

Hine, K. & Macnae, J. 2016, Comparing induced polarization responses from airborne inductive and galvanic ground systems: lewis Ponds, New South Wales, *Geophysics,* **81**(6), B179–B188.

Kaminski, V. & Viezzoli, A. 2017, Modeling induced polarization effects in helicopter time-domain electromagnetic data: field case studies, *Geophysics,* **82**(2), B49–B61.

Lane, R., Green, A., Golding, C., Owers, M., Pik, P., Plunkett, C. & Thorn, B. 2000, An example of 3D conductivity mapping using the TEMPEST airborne electromagnetic system, *Explor. Geophys.,* **31**(1–2), 162–172.

Lee, T. 1981, Transient electromagnetic response of a polarizable ground, *Geophysics,* **46,** 1037–1041.

Ley-Cooper, A.Y., 2019. Acquisition of geophysical data at a continental scale, *AGU Fall Meeting Abstracts,* **2019,** NS43D–0855.

Ley-Cooper, A.Y. & Brodie, R.C. 2013, Inversion of SPECTREM AEM data for conductivity and system geometry, *SEG Extended Abstracts,* **2013**(1), 1–4.

Lin, C., Fiandaca, G., Auken, E., Couto, M.A. & Christiansen, A.V. 2019, A discussion of 2D induced polarization effects in airborne electromagnetic and inversion with a robust 1D laterally constrained inversion scheme, *Geophysics,* **84,** E75–E88.

Lorentzen, T.H., Kass, M.A., Scheer, J., Tomaškovičová, S., Christiansen, A.V., Maury, P.K. & Ingeman-Nielsen, T. 2024, Exploring the challenges of interpreting near-surface towed TEM data on saline permafrost, *Geophysics,* **89**(3), E113–E128.

Macnae, J. 2016a, Quantitative estimation of intrinsic polarization and superparamagnetic parameters from airborne electromagnetic data, *Geophysics,* **81**(6), E433–E446.

Macnae, J. 2016c, Quantifying airborne induced polarization effects in helicopter time domain electromagnetics, *J. Appl. Geophys.,* **135,** 495–502. ISSN 0926-9851.

Macnae, J., 2016b, Airborne IP detects only fine-grained minerals when compared to conventional IP, *ASEG Extended Abstracts,* **2016**(1), 1–4.

Macnae, J., 2025, A physical interpretation of Cole–Cole equations and their ambiguous time constants for induced polarization models, *Geophys. J. Int.,* **243**(2), ggaf362.

Marchant, D., Haber, E. & Oldenburg, D. 2014, Three-dimensional modeling of IP effects in time-domain electromagnetic data, *Geophysics,* **79**(6), E303–E314.

Martin, T. & Weller, A. 2023, Superposition of induced polarization signals measured on pyrite–sand mixtures, *Geophys. J. Int.,* **234**(1), 699–711.

Minsley, B.J., Rigby, J.R., James, S.R. *et al.* 2021, Airborne geophysical surveys of the lower Mississippi Valley demonstrate system-scale mapping of subsurface architecture, *Commun. Earth Environ.,* **2,** 131.

Mulè, S. & Smiarowski, A. 2013, Evolution of TEMPEST–Bird positioning, in *ASEG-PESA Conference and Exhibition, 11-14 August 2013* Melbourne Australia.

Pelton, W.H., Ward, S.H., Hallof, P.G., Sill, W.R. & Nelson, P.H. 1978, Mineral discrimination and removal of inductive coupling with multifrequency IP, *Geophysics,,* **43**(3), 588–609.

Pittard, K. & Bourne, B. 2007, The contribution of magnetite to the induced polarization response of the Centenary orebody, *Explor. Geophys.,* **38**(3), 200–207.

Pitts, B., Dauti, F., Devkurran, N. & Viezzoli, A. 2021, AIP Effects in Airborne EM fixed wing systems: a SPECTREM theoretical case study, in *Australasian Exploration Geoscience Conference AEGC2021, 13-17 September 2021, Virtual Conference*.

Ray, A. 2021, Bayesian inversion using nested trans-dimensional Gaussian processes, *Geophys. J. Int.,* **226**(1), 302–326.

Smith, R.S. & Klein, J. 1996, A special circumstance of airborne induced polarization measurements, *Geophysics,* **61**(1), 66–73.

Spies, B.R. 1974, *Transient Electromagnetic Tests, Northern Territories and Queensland, 1972,* Bureau of Mineral Resources, Geology and Geophysics.

Spies, B.R. 1980, A field occurrence of sign reversals with the transient EM method, *Geophys. Prospect.,* **28,** 620–632.

Tarantola, A. & Valette, B. 1982, Generalized nonlinear inverse problems solved using the least squares criterion, *Rev. Geophys.,* **20**(2), 219–232..

Van Voorhis, G.D., Nelson, P.H. & Drake, T.L. 1973, Complex resistivity spectra of porphyry copper mineralization, *Geophysics,* **38,** 49–60.

Viezzoli, A. & Manca, G. 2019, On airborne IP effects in standard AEM systems: tightening model space with data space, *Explor. Geophys.,* **51**(1), 155–169.

Viezzoli, A. 2023, Lessons learned from a decade of AIP modelling, in *AEM2023–8th International Airborne Electromagnetics Workshop, 3-7 September 2023,* Fitzroy Island, QLD, Australia,

Viezzoli, A., Dauti, F. & Wijns, C. 2021, Robust scanning of AEM data for IP effects, *Explor. Geophys.,* **52**(5), 563–574.

Viezzoli, A., Kaminski, V. & Fiandaca, G. 2017, Modeling induced polarization effects in helicopter time domain electromagnetic data: synthetic case studies, *Geophysics,* **82**(2), B49–B61.

Ward, A.S. & Hohmann, A.G. 1988, *Electromagnetic Methods in Applied Geophysics: volume 1, Theory, 4. Electromagnetic Theory for Geophysical Applications,* pp. 130–311, eds Nabighian, M. N. & Corbett, J. D., SEG. https://library.seg.org/doi/abs/10.1190/1.9781560802631.ch4

Weidelt, P. 1982, Response characteristics of coincident-loop transient electromagnetic systems, *Geophysics,* **47**(9), E1325–1330.

Weller, A., Slater, L. & Nordsiek, S. 2013, On the relationship between induced polarization and surface conductivity: implications for petrophysical interpretation of electrical measurements, *Geophysics,* **78,** D315–D325.

Wilford, J.R., Searle, R., Thomas, M., Grundy, M.J. & Pagendam, D. 2016, A regolith depth map of the Australian continent, *Geoderma,* **266,** 1–13.